

Effect of 3D printing angle on microstructure and mechanical properties of silica ceramic cores by stereolithography

Yue Gu^{1,2}, *Wen-yan Duan¹, **Gong Wang¹, Bing-shan Liu¹, Xiao-dong Liu¹, and Shan Li¹

1. Key Laboratory of Space Manufacturing Technology (SMT), Technology and Engineering Centre of Space Utilization, Chinese Academy of Sciences, Beijing 100094, China

2. University of Chinese Academy of Sciences, Beijing 100049, China

Copyright © 2025 Foundry Journal Agency

Abstract: Ceramic cores fabricated by stereolithography exhibit great potential in casting turbine blades. Previous research on ceramic core molding was primarily conducted using vertical printing techniques, which not only resulted in lengthy molding durations but also compromised the mechanical strength. In this work, silica (SiO₂) ceramic cores, with fine complex geometric shapes, were fabricated using 65vol.% ceramic slurry by digital light processing (DLP) with different printing angles. Printing angles significantly impact the surface accuracy, shrinkage, printing efficiency of green bodies, as well as the microstructure and mechanical properties of sintered ceramic core samples. As the printing angle in the green body increases, the bonding area decreases, surface roughness on the XY plane worsens, shrinkage in the Z direction becomes more pronounced, and the printing efficiency declines. Similarly, an increase in the printing angle in the sintered body leads to a reduction in bending strength. At a printing angle of 30°, the printing time is reduced to half of that at 90°, which improves the molding efficiency. Meanwhile, the obtained bulk density of 1.71 g·cm⁻³, open porosity of 24%, and flexural strength of 10.6±1 MPa can meet the requirements of sintered ceramic cores. Therefore, designing and optimizing the printing angles can achieve the balance between shrinkage, printing efficiency, and flexural strength.

Keywords: silica; ceramic core; digital light processing; printing angle; mechanical properties

CLC numbers: TG221

Document code: A

Article ID: 1672-6421(2025)05-534-11

1 Introduction

With the development of modern industrial manufacturing technology and the improvement of aero-engine performance^[1], the products are increasingly required to be more precise and complex. Single crystal superalloy hollow blades with complex cavity cooling structures are increasingly urgent^[2, 3]. As an important part of hollow precision and complex

casting, the ceramic core has become one of the core elements in modern industrial manufacturing technology^[4-6]. Ceramic cores are generally molded by injection molding^[7, 8]. However, when producing ceramic cores with complex structures, hot injection molding technology faces the challenges of complicated processes, long production cycles, and high costs^[9, 10]. In addition, limited by traditional molding methods, ceramic cores have approached the upper limit of achievable geometric complexity, making it increasingly difficult to fabricate components with complex structures^[11, 12].

Stereolithography 3D printing ceramic technology is widely used to compensate for the limitations of traditional thermal injection processes in the preparation of complex core materials^[13, 14]. Given the unique capabilities of 3D printing, industrial and academic interests in 3D printing complex shaped castings such as ceramic cores are booming^[15-17]. The printing technology provides a feasible technique

*Wen-yan Duan

Female, born in 1989, Ph. D., Associate Professor. Research interests: Ceramic 3D printing technology, wave-transparent, wave-absorbing, and shielding materials/components. To date, she has published more than 60 academic papers.

E-mail: dwy@csu.ac.cn

**Gong Wang

Male, born in 1980, Ph. D., Professor. Research interests: Space manufacturing technology, 3D printing process and equipment for ceramics.

E-mail: wanggong@csu.ac.cn

Received: 2024-12-29; Revised: 2025-02-01; Accepted: 2025-03-03

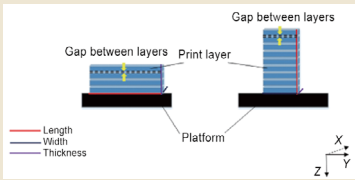
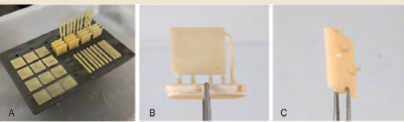
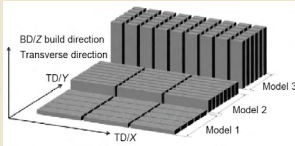
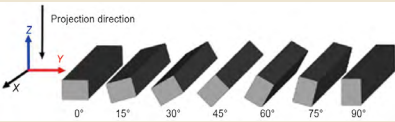
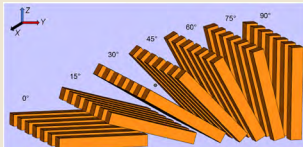
for preparing ceramic cores with complex structures^[7, 18] due to its many advantages including high design flexibility, customizability, mold free manufacturing^[19], reduced material waste, shorter production cycles^[20], ability to control porosity, and improved mechanical properties^[21, 22]. Therefore, ceramic cores with high performance^[23], high precision^[24], high bending strength^[25], and reduced production cost can be manufactured through stereolithography technology. This approach offers a promising route for the rapid manufacturing of high-complexity, high-quality ceramic cores essential for producing hollow turbine blades^[26].

In recent years, the photopolymerization 3D printing ceramic core technology has attracted widespread attention. Many excellent comments and reports have extensively covered the development of photopolymerization 3D printing ceramic cores^[27]. Wang et al.^[28] investigated the influence of nano-silica content on the performance and microstructure of silica-based ceramic core materials. The apparent porosity and pore size of the ceramic core gradually decreased as both the nano-silica content and the bulk density increased. Zhang et al.^[29] optimized the curing parameters by analyzing photopolymerization 3D printing technology under different exposure energies. Additionally, a detailed study was conducted to evaluate the sintering behavior and printability of ceramic pastes, as well as the performance of printing units in additive manufacturing. Lastly, regarding the research on debinding and sintering, Zhao et al.^[30] investigated two control methods to reduce residual stress during the 3D printing process. The study examined the debinding and sintering process using

thermogravimetric analysis and analyzed the impact of sintering temperature, heating rate, and dwell time on residual stress. However, current research on photopolymerization 3D printing of ceramic cores is mainly focused on the development and optimization of ceramic core pastes^[31], curing parameters^[32], and debinding and sintering processes^[33].

The shaping angle refers to the inclination angle of the ceramic core during the 3D printing process. Table 1 summarizes the primary published studies on the printing orientation of ceramic cores to date. The reported printing angles in these works are primarily defined with respect to the *X*, *Y*, and *Z* directions of the build platform^[20, 34-36]. An et al.^[35] studied the ceramic core samples from the *X*, *Y*, and *Z* directions, and found the bulk strength had the biggest value of 10 MPa in the *Y* direction and the smallest value of 3 MPa in the *Z* direction. Shen et al.^[36] studied the influence of printing angles on flexural strength of ceramic parts. The samples were rotated along the *Y*-axis, and the molding structure and the printing efficiency were optimized by adjusting the printing angles, as shown in Table 1. Results showed that the flexural strength was the worst when the printing angle was 45°. At an adequate angle, ceramic core molding efficiency can be significantly improved without sacrificing abundant flexure strength. However, current research on shaping angles is relatively limited, which restricts the potential of photopolymerization 3D printing of ceramic cores. Therefore, research on shaping angles is of significant importance. The influence of different shaping angles on the quality of ceramic cores should be explored to find the optimal shaping angle parameters.

Table 1: Previous studies on printing angles of additive manufacturing process

Printing angles	Materials	Printing directions	Influences	References
	Ceramic	0°, 90°	Flexure strength	[20]
	Photoresin	0°, 90°	Color and translucency	[34]
	Ceramic	<i>X</i> , <i>Y</i> , <i>Z</i>	Flexure strength	[35]
	Ceramic	0°, 15°, 30°, 45°, 60°, 75°, 90°	Flexure strength	[36]
	Ceramic	0°, 15°, 30°, 45°, 60°, 75°, 90°	Surface accuracy, flexure strength, printing efficiency	This work

This research focuses on analyzing the influence of Z-axis-rotated print angles on the surface roughness, porosity, and flexural strength of ceramic cores prepared using digital light processing (DLP) 3D printing. It establishes quantitative interrelationships between printing orientation and properties of ceramic cores, identifies the optimal print angle, and enhances printing efficiency while ensuring the ceramic cores meet application requirements.

2 Experimental procedure

2.1 Materials

The ceramic slurry used in this work was composed of 65vol.% ceramic powder and 35vol.% photosensitive resin. The ceramic powder consisted of 80wt.% SiO_2 and 20wt.% Al_2O_3 . Two SiO_2 powders with different particle sizes were used, characterized by D_{50} values of 5.8 μm and 21 μm , respectively. The powders were blended in a mass ratio of 7:3 (5.8 μm :21 μm). The photoresin mixture was consisted of 80wt.% monofunctional monomer (5-ethyl-1,3-dioxan-5-yl) (CTFA) and 20wt.% prepolymer, both received from Zhongshan Qianyou Chemical Material Co., Ltd. CTFA and prepolymer were ultraviolet curable acrylate resins with high photopolymerization activity and low shrinkage rate, which are suitable for DLP 3D printing. The dispersant was a copolymer with acidic groups. The photoinitiator (Irgacure 819) was purchased from Aladdin.

2.2 Preparation of ceramic slurry and green part printing

SiO_2 and Al_2O_3 particles, and dispersant (2wt.% of the total powder mass) were added to the photosensitive resin

(photoinitiator, 0.5wt.% of the total resin weight) and ball milled for 5 h in a planetary mill. The slurry was vacuum defoamed for 10 min to obtain the final ceramic slurry. Finally, a uniformly dispersed ceramic slurry with a solid content of 65vol.% was thereby obtained.

Samples with different printing angles (0° , 15° , 30° , 45° , 60° , 75° , 90°) were designed and the structures of the DLP printing samples are shown in Fig. 1. The ceramic green bodies were printed using a DLP 3D printer (Quickdemos Intelligent Manufacturing High-tech Co., Ltd., China). The printing layer thickness was 75 μm .

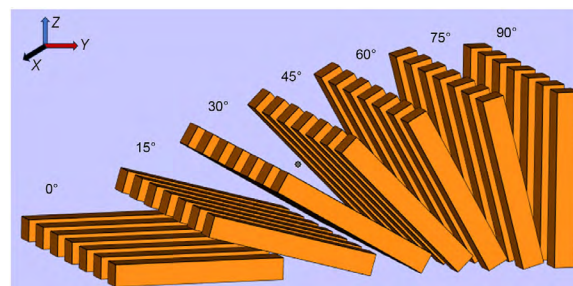


Fig. 1: Structure of DLP 3D printing samples

2.3 Debinding and sintering process

The printed green bodies were analyzed by thermogravimetry (TG) and derivative thermogravimetry (DTG) to determine the debinding and sintering process. Figure 2(a) shows the TG and DTG curves of green bodies. The samples exhibit two obvious weight loss stages. Figure 2(b) shows the schematic of photoresin decomposed from the printed sample, where the photosensitive resin was evaporated, leaving the ceramic powder. The green bodies after printing were debond in a muffle

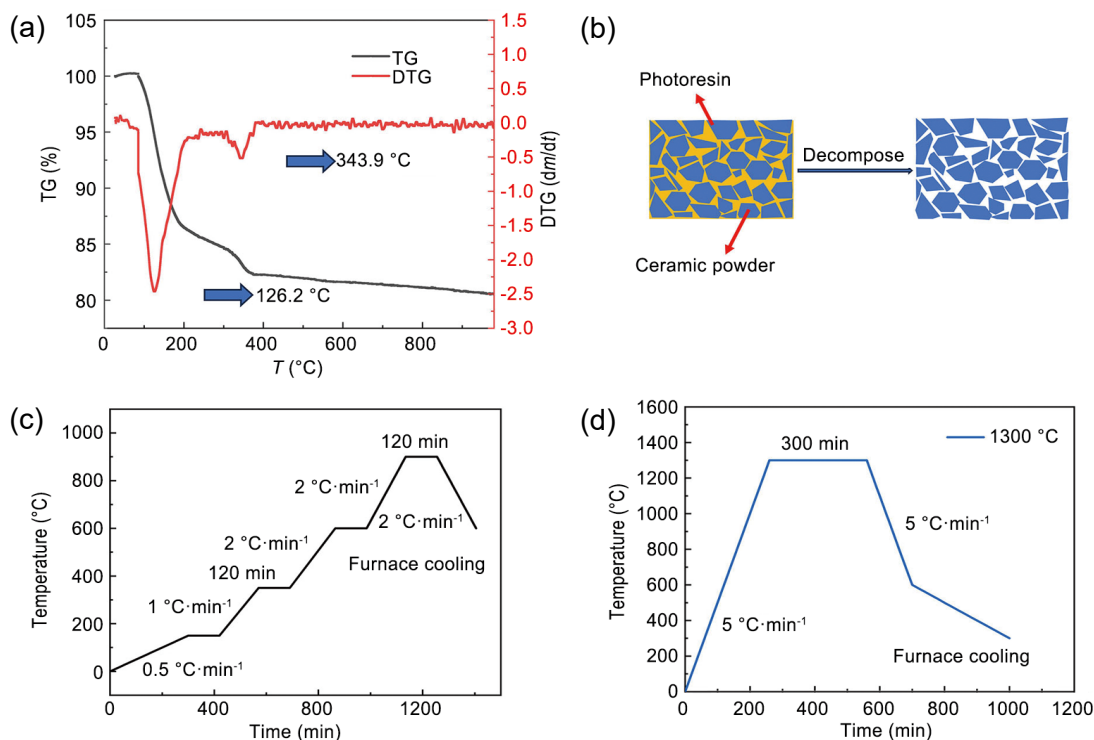


Fig. 2: TGA curves of the ceramic slurry (a), schematic of resin volatilization (b), debinding curve (c), sintering curve (d)

furnace (LT, Nabertherm, Germany). The detailed debinding process is shown in Fig. 2(c). The samples were then transferred to another muffle furnace (LT, Nabertherm, Germany) in an air atmosphere for sintering. Samples were heated to 1,300 °C at 5 °C·min⁻¹, held for 5 h, and then cooled to 600 °C at 5 °C·min⁻¹. The sintering process is illustrated in Fig. 2(d).

2.4 Characterization

The viscosity of the ceramic slurry with different shear rates was tested using a rheometer (Brookfield-Rheocalc-T). The surface roughness of ceramics after sintering was tested using the high-precision portable roughness gauge (SF200 Basic). The average size and size distribution of ceramic powder were analyzed using a laser particle size analyzer (Winner 2000ZDE). The weight loss behavior of the slurry during heating was investigated using the thermogravimetric analysis (TGA) (NETZCH STA 449F5) system from room temperature to 1,300 °C in the air at a heating rate of 10 °C·min⁻¹. The density and porosity of ceramic samples were measured by the Archimedes method. The microstructures of ceramic powder and the micrographs of the printed samples were observed using an SEM (Hitachi S-8020) with an accelerating voltage of 5 kV. The bending test in the three-point bending configuration was carried out on an Instron 5965 universal testing machine (Instron Co., Ltd., MA, USA). The loading speed was 0.5 mm·min⁻¹, and the span was 30 mm. During mechanical testing, the load was applied perpendicular to the sample surface (i.e., in the thickness direction). The sample was

measured 5 mm (width) × 5 mm (thickness) × 40 mm (length).

3 Results and discussion

3.1 Properties of ceramic slurry

The particle size distribution of SiO₂ and Al₂O₃ powder are shown in Figs. 3(a, d, and g). Figures 3(b, c), (e, f), and (h, i) are the SEM micrographs of SiO₂ and Al₂O₃ powders, respectively. SiO₂ powder exhibits an irregular shape with a relatively broad particle size distribution ranging from 1 μm to 100 μm. Al₂O₃ powder is spherical with a relatively narrow particle size distribution ranging from 100 nm to 6 μm.

The viscosity of the ceramic slurry is an important factor affecting whether the slurry can spread evenly on the printing platform. The variation in viscosity of ceramic slurry with different shear rates is shown in Fig. 4. The viscosity is relatively high at lower shear rates, and then decreases significantly with an increase in shear rate. When the shear rate reaches 100 s⁻¹, the viscosity decreases to 3,000 cP. The ceramic slurry shows good thixotropy, which is suitable for printing^[37].

The impact of exposure energy on the curing depth of ceramic slurry can be assessed by examining the curing depth at various light intensities. The findings are shown in Fig. 5(a), the curing depth of ceramic slurry increases from 180 μm to 280 μm with an increase in light intensities. Considering the printing thickness during the molding process is 75 μm, 55.2 mW·s·cm⁻² is chosen to be the exposure energy. The curing

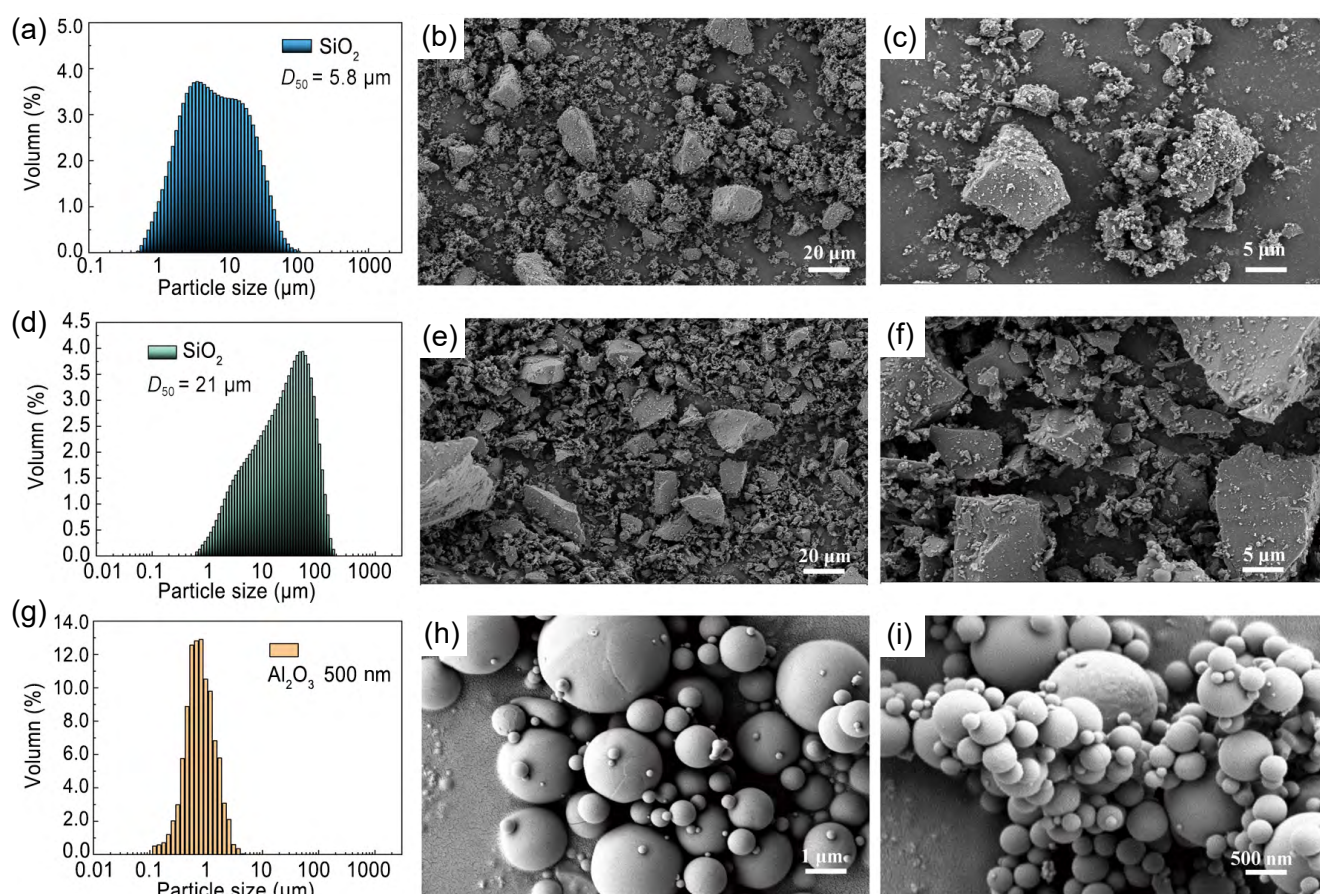


Fig. 3: Particle size distribution (a, d, g) and SEM micrographs (b, c, e, f, h, i) of ceramic powders

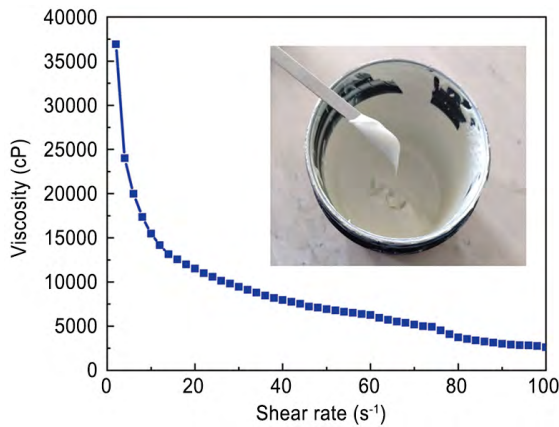


Fig. 4: Viscosity of ceramic slurry at different shear rates

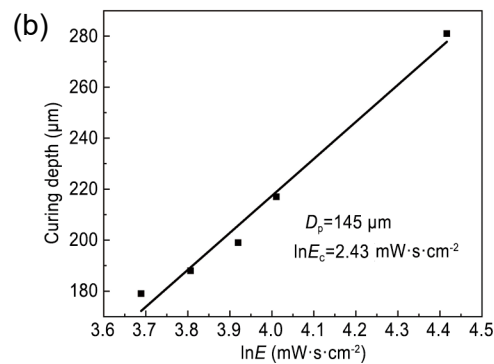
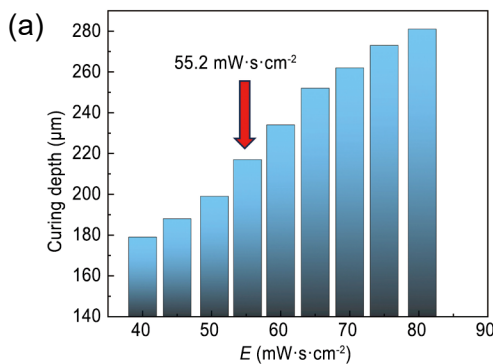


Fig. 5: Curing depth of ceramic slurry under different exposure energy

3.2 Influence of printing angle on accuracy of green body molding

The microscope images of the XZ plane in green body are shown in Fig. 6, as the layer thickness is the same in the DLP process of different printing angles. When the printing angle is 0° , the XY plane is parallel to the printing plane, while, when the printing angle is 15° , the XY plane interlayer bonding distance is much larger than the printing layer thickness, which is $289 \mu\text{m}$. With further increasing the printing angle, the interlayer distance on the XY plane is gradually reduced, as shown in Fig. 6, where the blue lines illustrate this distance. When the printing angle reaches 90° , the interlayer distance on the XY plane is equal to the printing layer thickness of $75 \mu\text{m}$.

The surface roughness of the XY plane is shown in Fig. 7. At a printing angle of 0° , the roughness is minimal, less than $1 Ra$, whereas at a printing angle of 15° , the roughness reaches its maximum value $5.9 Ra$. However, as the printing angle further increases, the roughness gradually decreases. At a printing angle of 90° , the roughness is $2.15 Ra$. These roughness results align with the observations using the microscope in Fig. 6 for the same system, indicating that the XY plane is flat at 0° and 90° .

Figure 8 shows the shrinkage of the green body in the X , Y , and Z directions fabricated at different printing angles. Different printing angles correspond to different cross-sectional areas of photocuring. At a printing angle of 0° , the shrinkage of the green body is minimal, with the bottom of the part adhering to the print platform, resulting in minimal shrinkage

depth and exposure energy can be modeled by the Beer-Lambert law, as shown in Eq. (1)^[38]:

$$C_d = D_p \ln \left(\frac{E}{E_c} \right) \quad (1)$$

where E is the exposure energy supplied by the laser beam. The penetration length (D_p) and critical exposure energy (E_c) are constant for the ceramic slurry, which can be determined by fitting the curing depth versus logarithmic exposure energy data based on the Beer-Lambert law. In the linear fitting equation, the slope corresponds to D_p , and E_c can be derived from the intercept. Therefore, D_p is $145 \mu\text{m}$, and the E_c is $11 \text{ mW} \cdot \text{s} \cdot \text{cm}^{-2}$. When the light intensity is less than the critical exposure energy density, the slurry cannot be cured.

in the Z direction, while the X direction has a greater shrinkage rate than the Y and Z directions. At 15° , shrinkage in the Z -direction (build direction) reaches a maximum, coinciding with the largest cross-sectional area being exposed during photocuring. This results in significant contraction in Z -direction and expands in the X and Y directions. The results shown in Fig. 8 also indicate that as the printing angle increases, the shrinkage of the green body gradually increases when the printing angle exceeds 45° . To improve the surface accuracy of the part, non-contact supporting forming is adopted, where only the bottom of the part contacts the print platform, while the rest of the part is formed without support. Due to the inevitable curing shrinkage during photopolymerization, when the printing angle is 15° , the maximum shrinkage in the Z direction is 1%. The calculation method for the forming area is $S = (5/\sin x) \times 5$ (x means printing angle), and with an increase in the printing angle, the cured area decreases, resulting in decreased shrinkage in the Z direction compared to that at 15° , and the shrinkages between X , Y , and Z tend to be the same.

3.3 Influence of shaping direction on microstructure and properties

The XZ plane SEM micrographs of the samples after sintering at different printing angles are shown in Fig. 9, it can be seen that when the printing angle is 0° , the interlayer bonding is good, the large particles are uniformly distributed in the interlayer, and the thickness of the printed layer is uniform. As the printing angle increases, the number of printed layers increases, and the

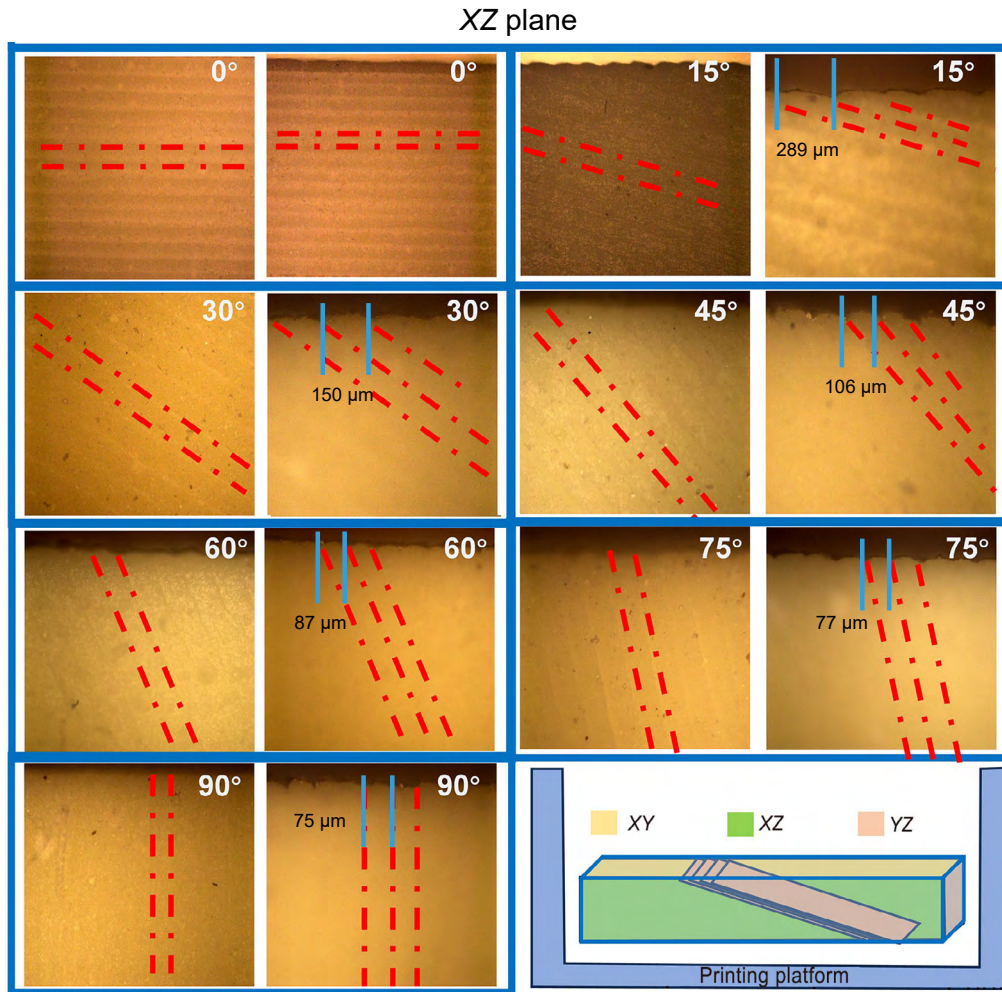


Fig. 6: Microscopic images of interlayer bonding of green body samples

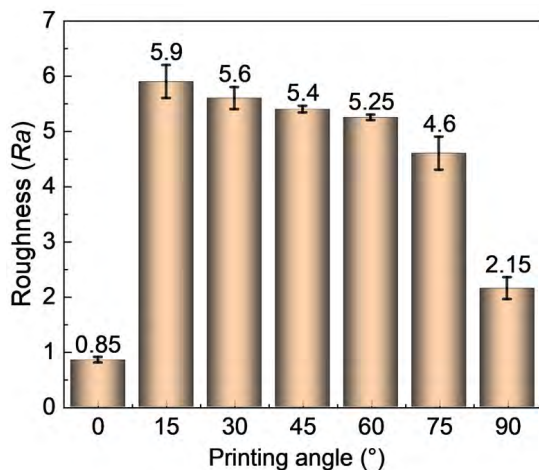


Fig. 7: Roughness of XY plane of green body samples

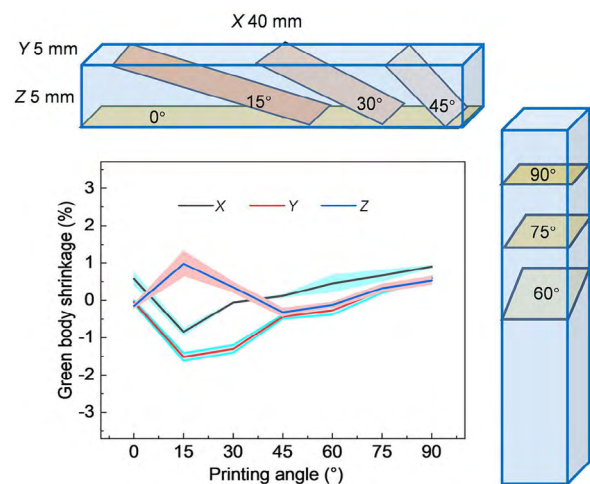


Fig. 8: Shrinkage of X, Y, and Z directions of green body samples printed by different angles

number of repeated layers of exposure increases. The thickness of the printed layer after sintering is markedly inhomogeneous, large particles appear to be deposited in the interlayer, and microcracks initiate. The number of microcracks increases with an increase in printing angle.

The SEM micrographs of the cross sections on XZ plane after sintering at different printing angles are shown in Fig. 10. It is observed that as the printing angle increases, the interlayer adhesion decreases. When the printing angle is less than 45°,

the inter-particle adhesion is strong, with alumina particles tightly bonded to quartz powder, exhibiting a smooth fracture surface and a transgranular fracture mode. In contrast, when the printing angle exceeds 45°, the interlayer adhesion weakens, and the alumina powder and quartz particles accumulate loosely, with evident cracks on the surface of the quartz particles. Moreover, with increasing printing angle,

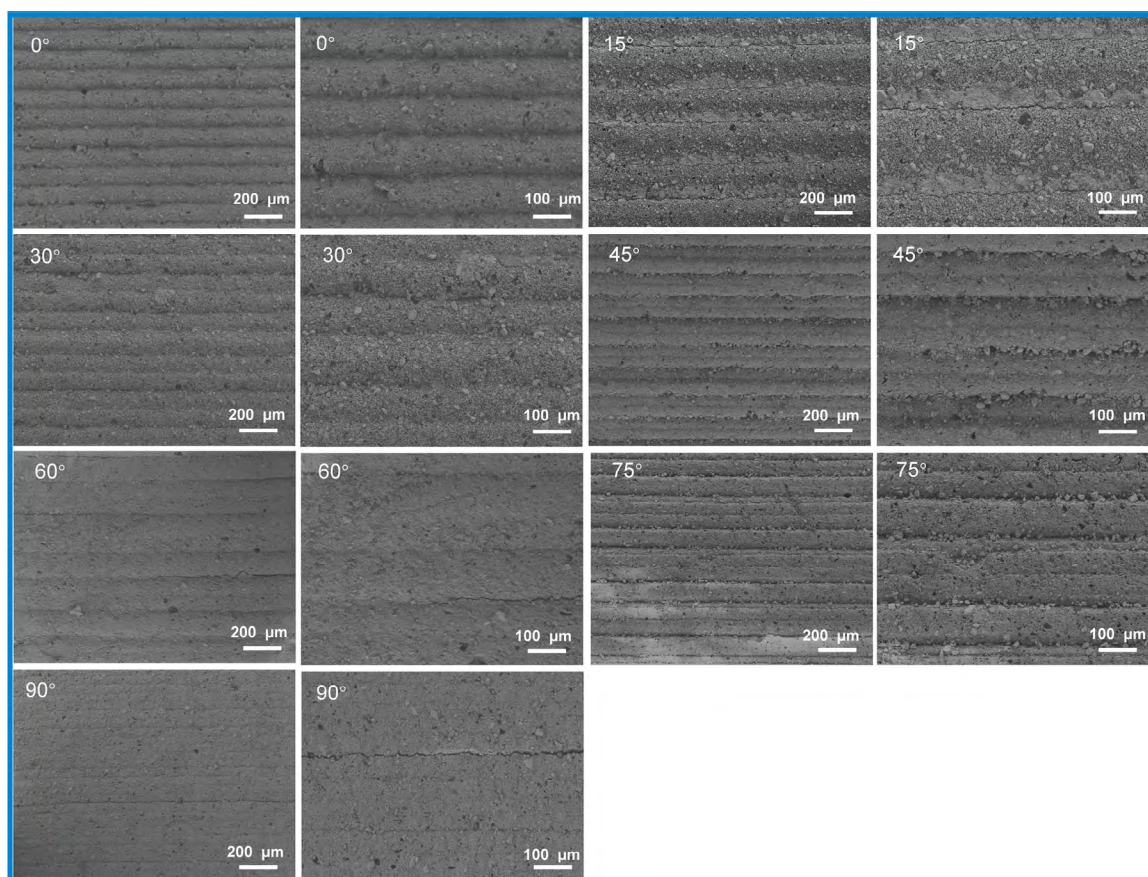


Fig. 9: SEM images of different layer thicknesses along XZ plane

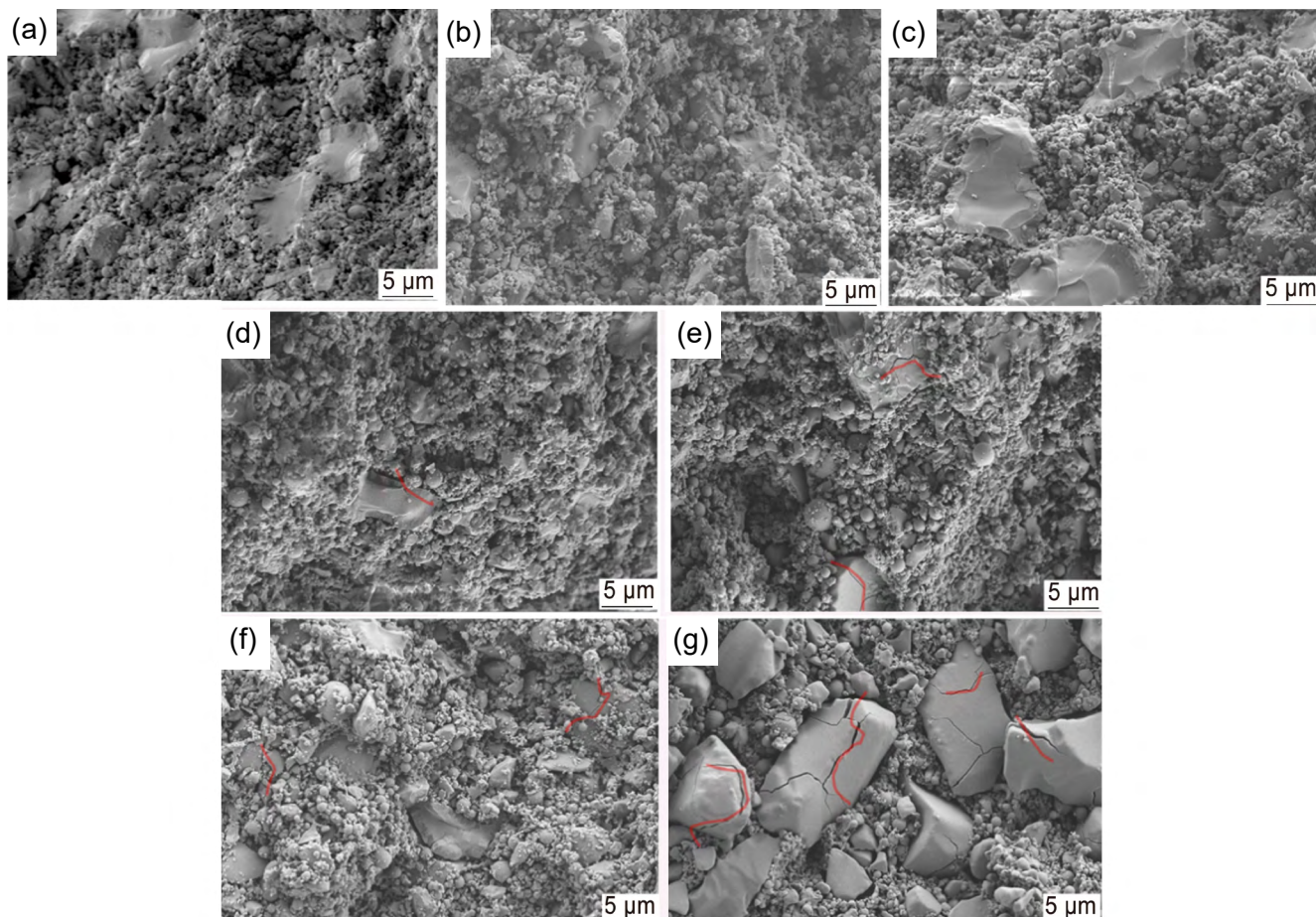


Fig. 10: SEM electron micrographs of cross section after sintering: (a) 0°; (b) 15°; (c) 30°; (d) 45°; (e) 60°; (f) 75°; (g) 90°

the number of cracks in the quartz increases significantly, with these micro-cracks acting as crack initiation sites during subsequent sintering and mechanical testing, evolving into a certain quantity of intergranular and intragranular cracks.

The sintered sample printing at 30° was analyzed using SEM microscopy and EDX elemental distribution. Figure 11(a) shows large particles with a diameter of $20\ \mu\text{m}$ surrounded by numerous small particles of $5\ \mu\text{m}$ in diameter and nano-sized particles. The subsequent elemental analysis results indicate the phase distribution in different regions, with a schematic shown in Fig. 11(b). Figure 11(c) lists the content of different elements, with Al content exceeding 10%, while the content of Si and O elements is comparable. This is similar to the proportion of elements in the raw materials. In addition, Figs. 11(d), (e), and (f) show the distribution of Si, O, and Al elements. It can be concluded that both the $20\ \mu\text{m}$ particles and the surrounding $5\ \mu\text{m}$ particles are silicon oxide particles. Furthermore, the sintering process results in the formation of

silicon and aluminum compounds, with Al elements distributed around the silicon oxide particles.

Shrinkage, density, and porosity of the sintered samples are shown in Fig. 12. The shrinkage at X, Y, and Z directions between different printing angles is similar, which is close to 5% in the X direction, 3.5% in the Y direction, and 3% in the Z direction. The effect of printing angle on the shrinkages of the sintered samples is much smaller than that of the green body. The printing angle has almost no effect on the density and porosity of the sintered samples; the average density after sintering is $1.77\ \text{g}\cdot\text{cm}^{-3}$, and the average porosity is 24%. Since the samples with different printing angles were fabricated using identical processing parameters, this further validates the minimal impact of printing angles on porosity and density.

Figure 13(a) shows the mechanical testing results of sintered samples fabricated by different printing angles. The flexural strengths are similar in both vertical and parallel directions, indicating good interlayer bonding of the specimens. The

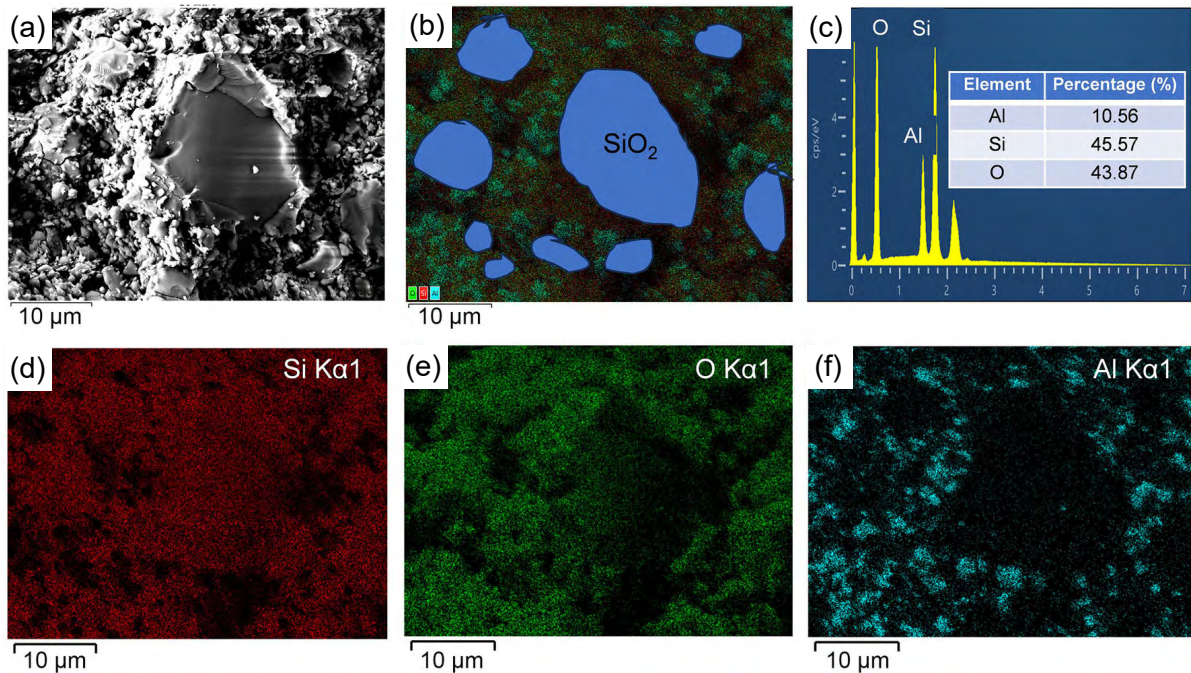


Fig. 11: Cross-section SEM image (a) and elemental distribution maps (b, c, d, e, f) of sintered samples with a printing angle of 30°

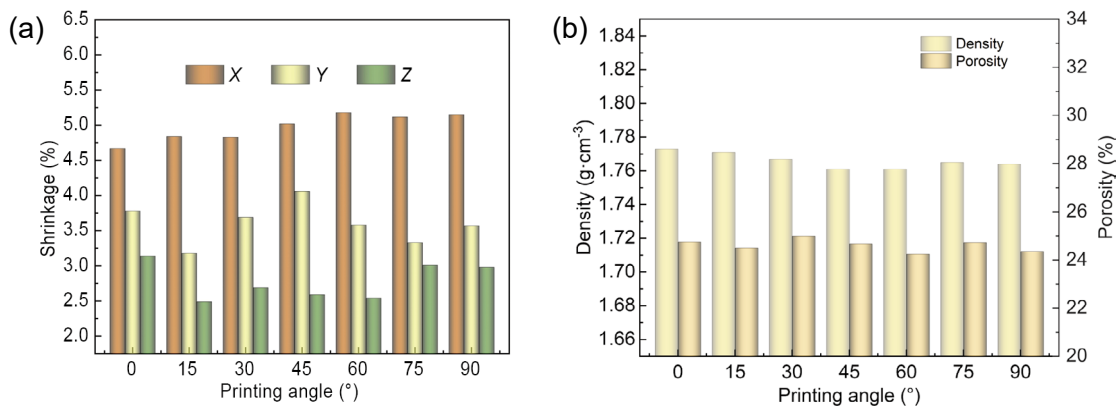


Fig. 12: Shrinkage of X, Y, and Z directions (a) and density and porosity of sintered samples printed by different angles (b)

strength test results at different printing angles reveals that as the printing angle increases, the flexural strength decreases. The flexural strength gradually decreases with the increase in the printing angle, from 18.5 MPa at 0° to 4.89 MPa at 90° along vertical direction. When the printing angle exceeds 30°, the flexural strength decreases by more than 50%. As shown in Fig. 13(b), when the angle exceeds 15°, the cracks in the sample mainly propagate along the printing direction. When the printing angle exceeds 30°, the flexural strength is less than 10 MPa, lower than the strength required for ceramic core use, hence the printing angle should be no more than 30°. After sintering, a span of 30 mm sample was chosen for the three-point bending mechanical testing. Observation of the samples after the three-point bending test reveals that when the printing angle is greater than 30°, the direction of fracture follows the printing angle, as shown in Fig. 13(b). Figure 13(c) illustrates the interlayer fracture mechanism. It can be observed that when the printing angle is 0°, the fracture direction exhibits a stepped fracture along the Z-axis direction. As the printing angle increases, the fracture direction aligns closely with the printing direction. Due to the increase in the printing angle, the interlayer bonding area decreases, resulting in reduced interlayer bonding strength.

3.4 Optimization of printing angles

Printing angles have an enormous influence on the quality

of ceramic shaping. Smaller printing angles can enhance the strength and rigidity of the core, making it more capable of withstanding external forces. Larger shaping angles can reduce the strength and rigidity of the core, making it more susceptible to damage or deformation. Therefore, when determining the shaping angles, it is necessary to consider both the operating environment of the core and the required mechanical performance. Smaller shaping angles can reduce resistance and material loss during the shaping process, thereby improving the efficiency of shaping. Conversely, larger shaping angles can increase resistance and material loss during the shaping process, thereby decreasing the efficiency of shaping. Hence, in the process of core making, selecting appropriate shaping angles is crucial for improving shaping efficiency.

The relationship between the printing angle and the molding method is displayed in Fig. 14. When the printing angle is 0°, the build direction is aligned with the Z-axis, resulting in the minimum projected area and the highest fabrication efficiency. However, the bottom surface of the core is an irregularly curved geometry, making support attachment difficult and increasing the risk of print failure due to delamination or collapse. When the printing angle is 90°, the build direction is perpendicular to the Z-axis, resulting in the largest projected area per layer and the lowest fabrication efficiency, and the mechanical strength of molding is low. When the printing angle is 30°, supports can be added at the bottom of the

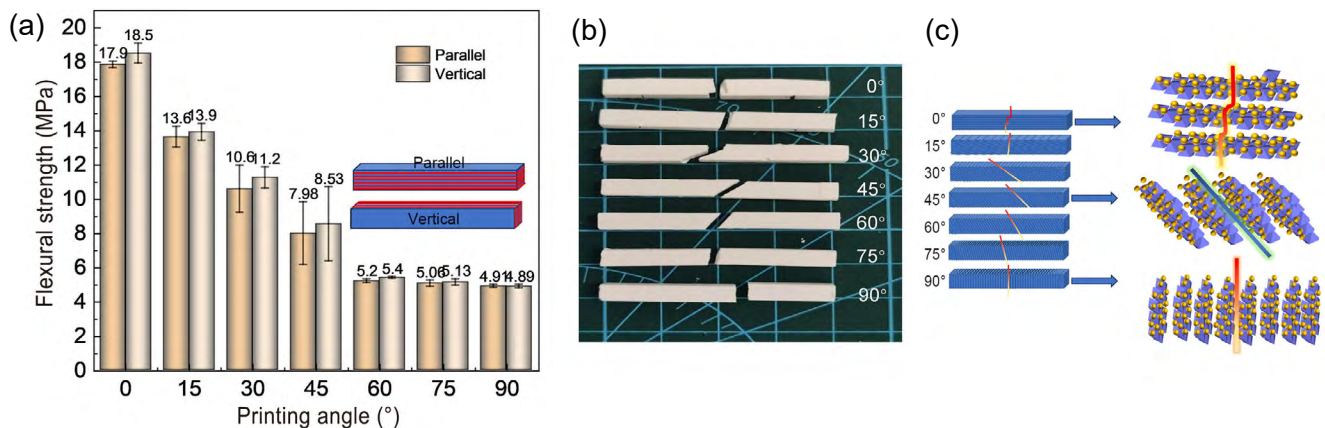


Fig. 13: Flexure strength of sintered samples in parallel and vertical directions (a), images of broken samples (b), schematic diagram of fracture mechanism (c)

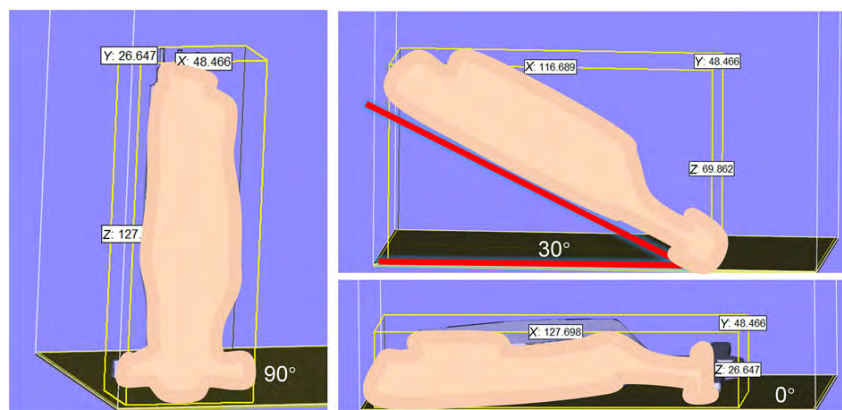


Fig. 14: Relationship between printing angle and molding method

model. This not only improves forming efficiency compared to printing at 90° and increases the printing success rate but also ensures that the flexural strength after sintering meets the required application standards.

4 Conclusion

This work explored the influence of printing angles on the surface accuracy, shrinkages, and printing efficiency in green body; and microstructure and flexural strength in sintered samples under the same sintering temperature of ceramic cores. At a printing angle of 15°, the *XY* plane surface roughness of the green body reaches its maximum value, and the sample exhibits the greatest shrinkage in the *Z* direction. The flexural strength of sintered samples decreases from 18.5 MPa at the printing angle of 0° to 4.89 MPa at 90° in vertical direction. Considering the printing efficiency and flexural strength, the printing angle of 30° is determined to be the best printing angle with shrinkage of 4.75%, 3.65%, and 3.05% in the *X*, *Y*, and *Z* directions; bulk density of 1.71 g·cm⁻³; open porosity of 24%; and flexural strength of 10.6±1 MPa. The relationship between printing angles and fracture mechanism was also discussed. The fracture direction exhibits a stepped fracture along the *Z*-axis direction at printing angle of 0°, as the printing angle increases from 15° to 90°, the fracture direction aligns closely with the printing direction.

Acknowledgments

The authors gratefully acknowledge the Youth Innovation Promotion Association of Chinese Academy of Science (No. 2021160), the National Natural Science Foundation of China (No. 51802319), and the Technology and Engineering Center for Space (No. CSU-QZKT-2019-04).

Conflict of interest

The authors declare that they have no known competing financial interests or personal relationships that could have appeared to influence the work reported in this paper.

References

- [1] Wong D T W, Ngai E W T. The impact of advanced manufacturing technology, sensing and analytics capabilities, and planning comprehensiveness on sustained competitive advantage: The moderating role of environmental uncertainty. *International Journal of Production Economics*, 2023, 265: 109007.
- [2] Liu X, Han X, Yin G, et al. Design and processing of gas turbine blades based on additive manufacturing technology. *Micromachines*, 2023, 14: 1675.
- [3] Li Q, Chen T, Liang J, et al. Manufacturing of ceramic cores: From hot injection to 3D printing. *Journal of Materials Science & Technology*, 2023, 134: 95–105.
- [4] Mu Y, Chen J, An X, et al. Defect control in digital light processing of high-solid-loading ceramic core. *Ceramics International*, 2022, 48: 28739–28744.
- [5] Niu Y, Jiang W, Yang L, et al. Preparation of low-cost high strength soluble ceramic cores using heavy calcium carbonate by binder jetting and vacuum impregnation. *Journal of the European Ceramic Society*, 2023, 43: 7714–7720.
- [6] Yin Y, Wang J, Huang Q, et al. Influence of debinding parameter and nano-ZrO₂ particles on the silica-based ceramic cores fabricated by stereolithography-based additive manufacturing. *Ceramics International*, 2023, 49: 20878–20889.
- [7] Kim E H, Park H Y, Lee C, et al. Single crystal casting of gas turbine blades using superior ceramic core. *Journal of Materials Research and Technology*, 2020, 9: 3348–3356.
- [8] Li Q, Liang J, Zhang Y, et al. Fused silica ceramic core based on network-structured zircon design via 3D printing. *Scripta Materialia*, 2022, 208: 114342.
- [9] Lakhdar Y, Tuck C, Binner J, et al. Additive manufacturing of advanced ceramic materials. *Progress in Materials Science*, 2021, 116: 100736.
- [10] Wang X, Mei X, Wang X, et al. Picosecond laser trimming of ceramic cores with porous multi-scale particle microstructure. *Ceramics International*, 2022, 48: 7593–7604.
- [11] Zheng W, Wu J M, Chen S, et al. Improved mechanical properties of SiB₆ reinforced silica-based ceramic cores fabricated by 3D stereolithography printing. *Ceramics International*, 2022, 48: 21110–21117.
- [12] Ozkan B, Sameni F, Karmel S, et al. Binder stabilization and rheology optimization for vat-photopolymerization 3D printing of silica-based ceramic mixtures. *Journal of the European Ceramic Society*, 2023, 43: 1649–1662.
- [13] Li Q, Hou W, Liang J, et al. Controlling the anisotropy behaviour of 3D printed ceramic cores: From intralayer particle distribution to interlayer pore evolution. *Additive Manufacturing*, 2022, 58: 103055.
- [14] Fan J, Li Q, Jin F, et al. High solid loading, low viscosity stereolithography 3D printing ceramic cores slurry. *Ceramics International*, 2023, 49: 40705–40715.
- [15] Gao H, An J, Chua C K, et al. 3D printed optics and photonics: Processes, materials and applications. *Materials Today*, 2023, 69: 107–132.
- [16] Mu Y, Chen J, An X, et al. Effect of synergism of solid loading and sintering temperature on microstructural evolution and mechanical properties of 60 vol% high solid loading ceramic core obtained through stereolithography 3D printing. *Journal of the European Ceramic Society*, 2023, 43: 661–675.
- [17] Fan J, Xu X, Niu S, et al. Anisotropy management on microstructure and mechanical property in 3D printing of silica-based ceramic cores. *Journal of the European Ceramic Society*, 2022, 42: 4388–4395.
- [18] Li X, Liu Z, Niu S, et al. Controlled anisotropy in 3D printing of silica-based ceramic cores through oxidization reaction of aluminum powders. *Ceramics International*, 2023, 49: 24861–24867.
- [19] Zhou S, Mei H, Chang P, et al. Molecule editable 3D printed polymer-derived ceramics. *Coordination Chemistry Reviews*, 2020, 422: 213486.
- [20] Niu S, Luo Y, Li X, et al. 3D printing of silica-based ceramic cores reinforced by alumina with controlled anisotropy. *Journal of Alloys and Compounds*, 2022, 922: 166325.
- [21] Budharaju H, Suresh S, Sekar M P, et al. Ceramic materials for 3D printing of biomimetic bone scaffolds-current state-of-the-art & future perspectives. *Materials & Design*, 2023, 231: 112064.
- [22] Fei J, Rong Y, Zhu L, et al. Progress in photocurable 3D printing of photosensitive polyurethane: A review. *Macromolecular Rapid Communications*, 2023, 44: 2300211.
- [23] Li H, Hu K, Liu Y, et al. Improved mechanical properties of silica ceramic cores prepared by 3D printing and sintering processes. *Scripta Materialia*, 2021, 194: 113665.

- [24] Choi H H, Kim E H, Kim B G, et al. Improvement of ceramic core strength by combining 3D printing technology and an organic-inorganic conversion process using dual polymers. *Ceramics International*, 2021, 47: 17644–17651.
- [25] Zheng W, Wu J M, Chen S, et al. Improved mechanical properties of SiC fiber reinforced silica-based ceramic cores fabricated by stereolithography. *Journal of Materials Science & Technology*, 2022, 116: 161–168.
- [26] An X, Mu Y, Liang J, et al. Stereolithography 3D printing of ceramic cores for hollow aeroengine turbine blades. *Journal of Materials Science & Technology*, 2022, 127: 177–182.
- [27] Zhang F, Li Z, Xu M, et al. A review of 3D printed porous ceramics. *Journal of the European Ceramic Society*, 2022, 42: 3351–3373.
- [28] Wang X, Zhou Y, Zhou L, et al. Microstructure and properties evolution of silicon-based ceramic cores fabricated by 3D printing with stair-stepping effect control. *Journal of the European Ceramic Society*, 2021, 41: 4650–4657.
- [29] Zhang C, Luo Z, Liu C, et al. Dimensional retention of photocured ceramic units during 3D printing and sintering processes. *Ceramics International*, 2021, 47: 11097–11108.
- [30] Zhao L, Jiang Z, Zhang C, et al. Regulation of residual stress in stereolithography printing of ZrO₂ ceramics. *Ceramics International*, 2023, 49: 30801–30810.
- [31] Morita S, Iijima M, Chen Y, et al. 3D structuring of dense alumina ceramics using fiber-based stereolithography with interparticle photo-cross-linkable slurry. *Advanced Powder Technology*, 2021, 32: 72–79.
- [32] Gu Y, Duan W, Wang T, et al. Additive manufacturing of Al₂O₃ ceramic core with applicable microstructure and mechanical properties via digital light processing of high solid loading slurry. *Ceramics International*, 2023, 49: 25216–25224.
- [33] Bhandari S, Maniere C, Sedona F, et al. Ultra-rapid debinding and sintering of additively manufactured ceramics by ultrafast high-temperature sintering. *Journal of the European Ceramic Society*, 2024, 44: 328–340.
- [34] Espinar P C, Bona A D, Pérez G M D M, et al. The influence of printing angle on color and translucency of 3D printed resins for dental restorations. *Dental Materials*, 2023, 39: 410–417.
- [35] An X L, Liang J J, Li J G, et al. Sample selection for models to represent ceramic cores fabricated by stereolithography three-dimensional printing. *Journal of Materials Science & Technology*, 2022, 121: 117–123.
- [36] Shen M, Zhao W, Xing B, et al. Effects of exposure time and printing angle on the curing characteristics and flexural strength of ceramic samples fabricated via digital light processing. *Ceramics International*, 2020, 46: 24379–24384.
- [37] Bartolomeo C, Julien S, Tanguy L, et al. Digital light processing stereolithography of zirconia ceramics: Slurry elaboration and orientation-reliant mechanical properties. *Journal of the European Ceramic Society*, 2022, 42: 2974–2982.
- [38] Mitsoulis E. Fountain flow of pseudoplastic and viscoplastic fluids. *Journal of Non-Newtonian Fluid Mechanics*, 2010, 165: 45–55.